Implementation of In-Situ High-Temperature XAFS Experiments: Case of Praseodymium Oxide as an Oxygen Electrode in Low-Temperature Solid Oxide Cells

B. Lemieszek[a,*], A. Maximenko[b], L. Alluhaibi[b], B. Kamecki[c], P. Jasiński[a] and S. Molin[a]

[a]*Advanced Materials Centre, Faculty of Electronics, Telecommunications and Informatics, Gdańsk University of Technology, Narutowicza 11/12, 80-233 Gdańsk, Poland*
[b]*National Synchrotron Radiation Centre SOLARIS, Jagiellonian University, Czerwone Maki 98, 30-392 Kraków, Poland*
[c]*Department of Microwave and Antenna Engineering, Faculty of Electronics, Telecommunications and Informatics, Gdańsk University of Technology, Narutowicza 11/12, 80-233 Gdańsk, Poland*

Received: 15.12.2025 & Accepted: 11.03.2026

Doi: 10.12693/APhysPolA.149.S183 *e-mail: bartlomiej.lemieszek@pg.edu.pl

This article presents the initial results of in-situ high-temperature X-ray absorption spectroscopy measurements using hard X-ray radiation of oxygen electrodes of solid oxide cells. The ability to perform in-situ measurements, i.e., under conditions close to those of real operation, enables the acquisition of unique information on the behaviour of the material, providing a deeper understanding of the operating mechanisms of the electrodes, which can guide their further development. Praseodymium oxide (PrO_x) was selected as a promising material with potential applications in low-temperature solid oxide cells. The average oxidation state of praseodymium in a 100 nm PrO_x film has been shown to decrease from 3.49^+ at room temperature to 3.06^+ at 400°C. These results emphasise the importance of using thin films and highlight the processes occurring at the interface between the electrolyte (ionic conductor) and the oxygen electrode. The studies presented here lay the groundwork for further development in this area of high-temperature measurements, with the goal of establishing operando measurement methodology.

topics: in-situ, XANES, praseodymium oxide, solid oxide cells

1. Introduction

Solid oxide cells (SOCs) are among the most promising technologies for alternative energy generation and conversion. This is due to their high fuel flexibility, including hydrogen, methane, CO_2, ammonia, and other hydrocarbons, as well as their ability to operate in reversible modes. They can either generate electricity by converting the chemical energy stored in chemical bonds or produce fuel by reversing the reaction by changing the electrode polarity. One particularly important advantage of this technology is its potential to act as a zero-emissions energy source when hydrogen is used as the fuel, since the only byproduct of the reaction is water, which is environmentally harmless [1]. Another key benefit of SOCs is their high energy conversion efficiency, with electrical efficiencies in fuel cell mode reaching up to $\sim 60\%$, and system efficiencies in electrolyser mode around 80% when integrated into a cogeneration system. In addition, solid oxide electrolyser cells (SOECs) can operate at lower cell voltages than low-temperature electrolysers due to enhanced reaction kinetics at high operating temperatures [2–4].

However, several challenges must be addressed before the technology can achieve broad commercial adoption. In particular, reductions in production and operational costs are required, which are directly linked to the materials used and operating temperature. Currently, typical SOFC/SOEC stacks (SOFC — solid oxide fuel cell) operate in the temperature range of 700–900°C. Such high temperatures accelerate material degradation, increase costs due to the need for high-chromium steel interconnects, and reduce stack lifetime compared to low-temperature electrochemical systems [5, 6].

Several strategies are being pursued to resolve these issues and thereby lower the overall energy cost. The main approaches include identifying materials that maintain high performance in the

low-temperature SOC regime (below 600°C), reducing electrolyte thickness, and employing more economical material solutions that provide comparable performance [7]. Each of these approaches requires a comprehensive understanding of the materials used in SOCs. In this context, in-situ and operando measurements could play a crucial role, as they not only provide unique information unobtainable through ex-situ methods but also enable real-time monitoring of ongoing processes [8].

In this context, the application of in-situ and operando methods for describing materials and electrochemical mechanisms in the high-temperature range is becoming increasingly widespread. For example, operando measurements by Ma et al. [9] were performed using a setup that combined transmission electron microscopy (TEM) with electrochemical impedance spectroscopy. The experiments were conducted in a reactive gas environment (H_2 and H_2O) at elevated temperatures and under an applied electric potential. The main aim of the study was to demonstrate that such measurements are feasible, which required advanced sample preparation using focused ion beam–scanning electron microscopy (FIB-SEM). The authors successfully met this objective, thereby creating a foundation for future, more detailed investigations of electrochemical reactions, transport phenomena, and degradation mechanisms [9].

One technique of particular relevance is X-ray absorption fine structure (XAFS) spectroscopy. XAFS describes oscillations in the X-ray absorption coefficient that occur at energies up to approximately 1000–1500 eV above the absorption edge of the central atom. The fine structure is divided into two regions, namely XANES and EXAFS. The XANES region is dominated by low-energy, strongly multiple-scattered photoelectrons and is highly sensitive to oxidation state, site symmetry, and local geometry in the immediate coordination environment, with contributions that can also extend to somewhat longer-range interactions. The EXAFS region corresponds to higher photoelectron energies, where the de Broglie wavelength is shorter and single-scattering processes typically dominate. EXAFS analysis provides quantitative information on interatomic distances, coordination numbers, and the degree of static disorder within several coordination shells around the central atom [10].

In the context of SOC research, XAFS constitutes a powerful tool for comprehensive material characterisation and for detecting subtle structural and chemical changes. It enables, for example, the evaluation of dopant effects on crystal structure, the determination of oxidation states of electrochemically active species, the detection and analysis of degradation processes, and the characterisation of partially crystalline or fully amorphous phases [11, 12]. Additionally, wavelet transform analysis can be employed to identify subtle variations in local atomic arrangements and may provide insight into the mechanisms underlying changes in electrochemical performance [11, 13, 14].

Only a limited number of operando synchrotron-based studies have investigated SOCs. However, many of these rely on techniques other than X-ray absorption fine structure (XAFS). One example is the work of Acuña et al. [15], where the authors investigated a composite oxygen electrode made of $La_{0.6}Sr_{0.4}CoO_{3-\delta}$ (LSC) and $Ce_{0.8}Gd_{0.2}O_{2-\delta}$ (CGO), focusing on the effect of CGO particle size. The results showed that the average cobalt oxidation state decreases from 3.4^+ at room temperature to about 3.0^+ at 700°C. This reduction is linked to an increased concentration of oxygen vacancies and the formation of Co^{2+}, reaching a level comparable to that of Co^{4+}. It was further demonstrated that a lower average cobalt oxidation state can enhance the performance of the oxygen electrode [15]. In a recent work by Fujimaki et al. [16], a high-temperature operando micro-XAS (micro-X-ray absorption spectroscopy) method with spatial resolution < 1 μm was used for a developed cell, which allows for simultaneous control of the atmosphere, temperature, and electrochemical polarisation. It was also possible to directly determine the electrochemically active region in a porous SOFC cathode with an LSC on a CGO electrolyte. It was shown that under a cathodic overpolarisation of 140 mV at 873 K and $p(O_2) = 10^{-2}$ bar, the electrochemical reaction occurs only in a narrow region, approximately 1 μm from the electrode–electrolyte interface, despite the electrode itself being significantly thicker. This was confirmed by local changes in the effective oxygen partial pressure determined from the Co K-edge shift. This result experimentally confirms the predictions of Adler–Lane–Steele-type models of a strongly inhomogeneous reaction distribution in porous MIEC electrodes (MIEC — mixed ionic–electronic conductors) and indicates that the actual "active" part of the electrode is much thinner than its nominal thickness. The developed methodology can be used as a general tool to study the reaction distributions in other SOFC electrodes, electrolytic cells, and solid-state batteries [16].

One of the main challenges in the development of solid oxide cells is to produce oxygen electrodes that maintain high activity at intermediate and low operating temperatures. Reports suggest that the area-specific resistance of the oxygen electrode should not be much higher than 0.1–0.2 Ω cm^2 to ensure efficient operation [17]. Considering the materials typically used as oxygen electrodes in SOCs and their potential adaptation for low-temperature operation, several promising candidates should be highlighted. One of the most notable groups is the perovskite oxides LSC (i.e., $La_{1-x}Sr_xCoO_{3-\delta}$) and LSCF (i.e., $La_{1-x}Sr_xCo_{1-y}Fe_yO_{3-\delta}$) [11, 18–20]. LSC crystallises in a cubic perovskite structure and exhibits mixed conductivity, combining high electronic conductivity (around 100 S/cm at 600°C)

with significant ionic conductivity in the intermediate temperature range [21, 22]. This mixed conduction behaviour effectively increases the active surface area of the oxygen electrode, which represents a significant advantage over previously utilised electrode materials. However, both LSC and LSCF are characterised by a very high thermal expansion coefficient value, which reduces their compatibility with commonly used electrolytes [23]. Moreover, LSC and LSCF readily react with YSZ (yttria-stabilised zirconia), which requires the use of CGO ($Ce_{1-x}Gd_xO_{2-\delta}$) barrier layers [24, 25]. Additional challenges include rapid performance degradation due to strontium segregation, as well as sensitivity to humidity, which leads to the formation of strontium hydroxide — a reaction that partially irreversibly blocks active reaction sites [20, 26, 27]. Similar to LSC, LSCF also exhibits mixed conductivity. While its electronic conductivity is comparable to that of LSC, its ionic conductivity is lower within the same temperature range [18].

Another candidate for the low-temperature region that is currently attracting increased attention is praseodymium oxide (PrO_x). This material has recently emerged as a promising candidate for enhancing the catalytic activity of the oxygen reduction reaction in SOC applications. PrO_x is a noteworthy example among binary oxides because it can adopt a wide range of non-stoichiometric compositions that cannot be explained by isolated point defects alone. Instead, these compositions form extensive and highly interconnected structural arrangements, resulting in a complex network of defect interactions [28, 29]. As a mixed ionic–electronic conductor (MIEC), PrO_x exhibits a total conductivity of 6.77×10^{-2} S/cm at 400°C [30]. Its markedly lower electronic conductivity means the material is typically used as an addition to the base material. The most electrochemically active β-form of PrO_x — Pr_6O_{11} or $PrO_{1.833}$ — is stable at comparatively low temperatures of around 430°C. A slight increase in temperature to around 470°C promotes transformation into the other phases. In contrast, the ι-phase (often associated with Pr_7O_{12}, appearing at around 700°C) demonstrates significantly lower total conductivity [28, 30]. The pronounced structural variability of PrO_x, alongside the associated differences in physicochemical behaviour, highlights the need for careful optimisation of material parameters to enable its effective application in solid oxide cell systems [31].

2. Experimental setup

2.1. In-situ cell construction

The work involves the design, fabrication, and testing of a new type of measuring cell enabling in-situ measurements (high temperature) and, in future iterations, operando measurements (high temperature, atmosphere control, electrical connections). The measuring cell was designed using Autodesk Inventor. The design includes a sample base equipped with a gas flow distribution structure that allows access and gas exchange in the region adjacent to the electrode. The base dimension was defined as 16 mm. This dimension provides XANES spectra of adequate quality for analysis, while also optimising material consumption and allowing the use of a 19 mm hydraulic press mould for producing the electrolytic substrate, which contracts to 16 mm after high-temperature sintering. The small holes enable the provision of electrical contact using platinum wires, which serve as one side of the system for symmetrical measurements. Tubes were placed beneath the base to prevent direct contact between the wires. Additionally, a third tube for a thermocouple placement was embedded below the base. This configuration allows for direct temperature measurement at the sample, ensuring optimal measurement accuracy and process control. Further structural components were designed to integrate the heating elements. The assembly was fabricated via stereolithographic 3D printing (Tethon 3D BISON 1000) using a high-alumina ultraviolet-curable ceramic resin, which allows for the creation of geometrically complex parts with high dimensional accuracy. Dimensional shrinkage of approximately 20% during post-processing was accounted for during slicing in the 3D printing software.

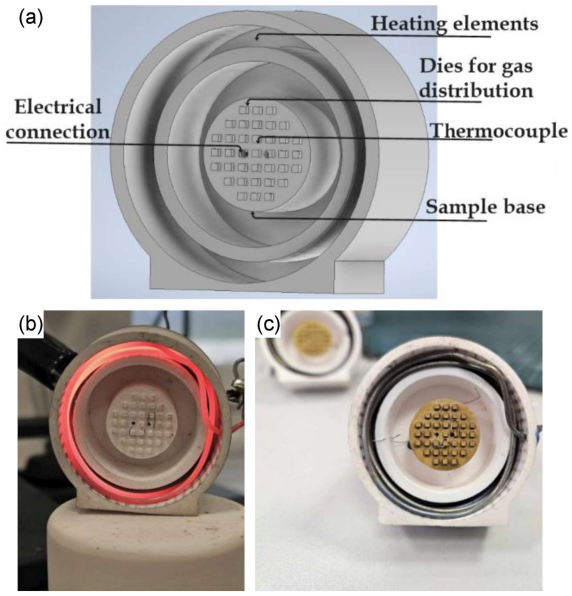

Fig. 1. Design of the measuring cell (a), the cell during heating tests (b), and the prepared cell for in-situ/operando measurements (c).

After printing, the components underwent purely thermal debinding and subsequent sintering in a high-temperature furnace (Czylok FCF 4/170M). The thermal profile included multiple heating

ramps, each defined by a heating rate and an associated dwell time: heating to 275°C at 135°C/h (no hold), subsequently to 338°C at 14°C/h with a 60 min hold, then to 500°C at 14°C/h with a 30 min hold, followed by 650°C at 135°C/h with a 15 min hold, and finally to 1700°C at 170°C/h with a 120 min hold to ensure full densification of the ceramic structure.

Kanthal wire was used for the heating element. The direct current (DC) power supply (Delta Elektronika SM15-100) was connected to the heating element. Initial calibration allowed for precise and stable temperature control via a thermocouple placed adjacent to the sample. This calibration was necessitated by the absence of PID control. As a result, heater and cooling power were not adjusted automatically, and temperature regulation relied entirely on user-defined settings. Preliminary tests of the completed circuit demonstrated the ability to reach temperatures of up to 950°C. Notably, no cracks or defects were observed during these tests, confirming the possibility of reusing the circuit even under rapid heating–cooling cycles. The principal design assumptions and the components incorporated in the measurement setup are summarised in Fig. 1a. The arrangement of components in the printed measurement cell is presented in Fig. 1b and c.

2.2. Sample preparation

Samples were prepared in a typical symmetrical electrode configuration, in which electrodes were deposited on each side of the electrolyte. The electrolyte substrates for the oxygen electrode layer were based on yttria-stabilised zirconia (YSZ). The pellets were produced by uniaxially pressing YSZ powder (Tosoh Corporation) at 98 MPa and sintering for 10 h in air at 1400°C. The resulting samples were disk-shaped, with an average diameter of ≈ 16 mm and a thickness of ~ 0.6 mm. YSZ pellets were polished before electrode application to obtain a smooth surface using a semi-automatic polisher (Struers Tegramin-20).

The PrO_x precursor was prepared by dissolving $Pr(NO_3)_3 \cdot 6H_2O$ (99.9% purity, Alfa Aesar) in distilled water to obtain a 0.25 mol/dm^3 solution. To this solution, 2-butoxyethanol (99% purity, Sigma Aldrich) was added in a 1:1 volume ratio with water, along with citric acid (99% purity, Chempur) as a chelating and oxidising agent at a 1:2 molar ratio vs the total metal ions (TMI). Finally, 5 wt% ethanol (99.8% purity, POCH) was added. The mixture was heated on a hotplate at 100°C with continuous stirring for ≈ 15 min to evaporate water and ethanol, reducing the solution volume by half.

The PrO_x oxygen electrode layer was deposited on the YSZ pellets using a spin-coating technique (Laurell spin coater, model WS-400B-6NPP/LITE). To the YSZ surface, 6 μL of the PrO_x precursor was applied, and excess solution was removed through a three-stage rotation sequence: 1000 rpm for 20 s, 3000 rpm for 30 s, and 5000 rpm for 30 s. After each coating step, the pellets were heated on a hotplate at 90, 180, and 400°C, holding each temperature for 15 min. The process was repeated two times per side, resulting in a final film thickness of ≈ 100 nm. The samples were not subjected to additional annealing; 400°C was the maximum processing temperature.

2.3. XAFS measurement methodology

X-ray absorption spectroscopy measurements at the Pr L_3-edge were carried out at the ASTRA beamline of the SOLARIS National Synchrotron Radiation Centre in Kraków, Poland. The white beam generated by the 1.3 mm bending magnet was monochromatised using a modified Lemonnier-type double-crystal monochromator equipped with a Ge(220) crystal pair. At the sample position, the monochromatised beam dimensions were 7 mm $\times$ 1 mm. XANES spectra were collected in fluorescence mode, with the sample chamber and ionisation chambers filled with air at atmospheric pressure. The monochromator energy calibration at the Pr L_3-edge was performed using a Cr foil from Exafs Materials (Danville, CA). The sample was placed in the measuring cell, which was subsequently enclosed within a double housing designed to minimise infrared radiation entering the chamber and thus limit unintended heating. The housings were fabricated from aluminium, a material with high infrared reflectivity. The window, designed to shield the detectors from direct thermal radiation, consisted of 60 μm-thick glassy carbon (SIGRADUR K film) from HTW Hochtemperatur Werkstoffe GmbH (Thierhaupten, Germany). The complete assembly is presented in Fig. 2. Further spectral analysis was conducted using the Athena software packages [32].

3. Results and discussion

3.1. Preparation of measurements, material consideration, and cell calibration

Ensuring stable measurement conditions with respect to the applied temperature was the first key aspect to be addressed. Accordingly, tests were performed on the measurement cell to establish a direct, practically applicable relationship. The procedure began with heating the cell to an elevated temperature to form an oxide layer on the heating element, thereby improving repeatability in subsequent runs. The next step was to determine target temperatures, set in 50°C increments from 200 to 600°C, and correlate them with the direct current (DC) supplied by the power supply.

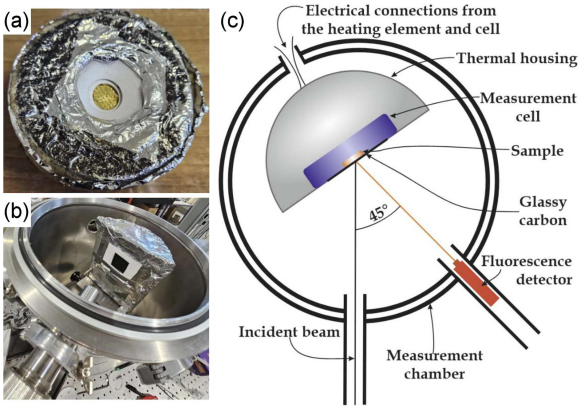

Fig. 2. The aluminium housing used for measurements at elevated temperatures (a), the final construction with the glassy carbon window placed in the measuring chamber (b), and a sketch of the construction and arrangement of elements during in-situ measurements (c).

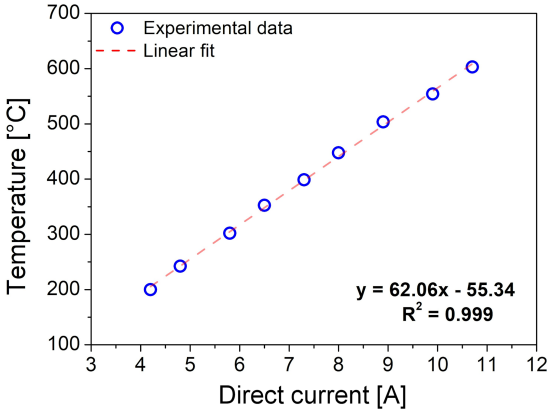

Fig. 3. Calibration curve defining the relationship between the direct current (DC) value of the power supply and the temperature of the measuring cell.

Each setpoint was held for 1 h to ensure thermal equilibrium and stable conditions for XANES acquisition, as spectrum collection and repeated scans can extend the measurement duration beyond 1 h. This approach provided sufficient stability for long experiments (e.g., assessments of how cell temperature influenced the overall temperature of the measurement chamber on the ASTRA beamline, where measurements at fixed temperatures continued for several hours). Figure 3 shows the calibration curve obtained from measurements conducted to determine the relationship between the DC supplied to the heating element and the resulting steady-state temperature. This curve was used to establish values enabling precise and accurate temperature control. Linearity was confirmed by the parameter R^2, whose value was close to 1. The fitted calibration equation allowed for the accurate determination of the DC required to achieve specific temperatures in the developed measurement system, thereby enabling in-situ measurements under stable and controlled conditions.

Another factor that had to be considered was the choice of the substrate for electrode deposition. Owing to the small thickness of the oxygen electrode, contributions from the substrate may overlap with the signal of the measured material. The selection of YSZ was dictated by the electrode materials used — in this case, praseodymium oxide. However, even when using cobalt-based electrochemically active materials, YSZ would remain necessary due to the absorption edge energies of cerium and gadolinium; these are 6164 eV and 5723 eV for the Ce L_2- and L_3-edges, and 7930 eV and 7243 eV for the Gd L_2- and L_3-edges, respectively. For praseodymium, the L_2- and L_3-edges occur at 6440 eV and 5964 eV, respectively, while cobalt exhibits a K-edge at 7709 eV. YSZ is therefore a safe choice, as its L_2- and L_3-absorption edges remain below 3000 eV — far from those of the materials under investigation — thus ensuring reliable spectral analysis.

3.2. Preliminary studies — preparation for in-situ measurements

XANES measurements of praseodymium oxide were performed in fluorescence mode. Each measurement was preceded by heating to the target temperature and stabilising at that temperature for 30 min. The measurements were carried out on thin praseodymium oxide electrode layers ($\sim$ 100 nm thick) deposited on a YSZ substrate (Fig. 4a). The layer thickness was determined by preliminary ex-situ measurements analysing the occurrence and magnitude of self-absorption. This effect arises from the fluorescence measurement mode; the recorded signal was not the attenuation of the incident beam, as in a standard transmission experiment, but the number of fluorescent photons emitted by the analysed element with a specific energy. When such a photon is generated inside the material, there is a finite probability that it will be re-absorbed within the sample (either by the same element or by other atoms in the matrix). As a consequence, the detected signal is attenuated because not all of the emitted fluorescence reaches the detector. This leads to a breakdown of the proportionality between the fluorescence intensity and the true absorption coefficient, and therefore to a distortion of the measured spectrum. Self-absorption causes a flattening of the absorption edge, a reduction and broadening of the white line, and an apparent increase in intensity just above the edge, corresponding to a flattening and compression of the XANES structure amplitudes. This effect is particularly important for the white line, which is commonly used

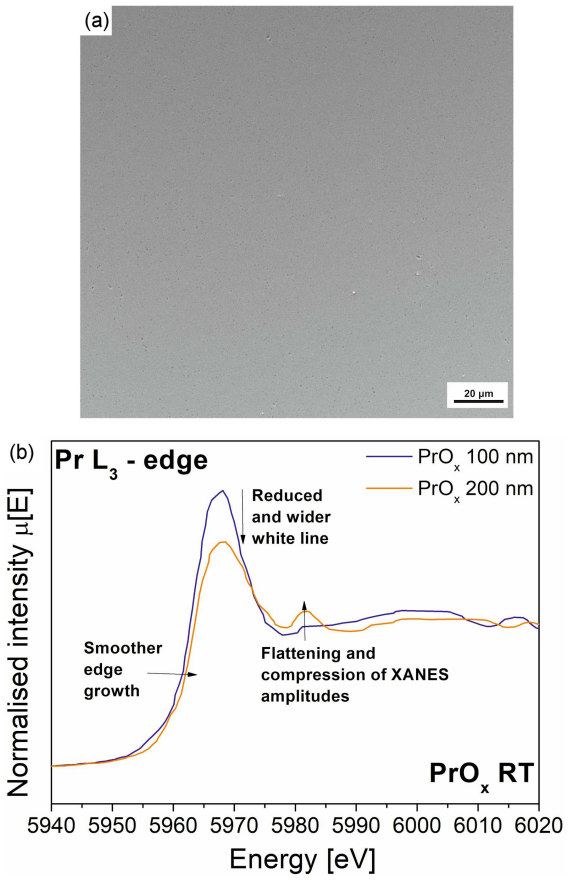

Fig. 4. SEM image of the surface of the PrO_x oxygen electrode (100 nm thick) deposited on the YSZ substrate (a), XANES spectra obtained for different thicknesses of praseodymium oxide defining the maximum thickness that can be used in measurements (b).

to determine the average oxidation state of the analysed element. In practice, self-absorption is most pronounced in fluorescence measurements of concentrated or undiluted samples and can often be neglected only for sufficiently thin or strongly diluted specimens. Figure 4b shows XANES spectra collected for praseodymium oxide layers with thicknesses of approximately 100 and 200 nm. All of the effects characteristic of self-absorption are observed for the 200 nm sample and are not present for the 100 nm layer. Furthermore, the data were compared with measurements performed on powdered praseodymium oxide annealed at the same temperature, confirming the absence of self-absorption under those conditions.

3.3. In-situ measurements

In-situ measurements provide much more extensive and representative information about the material, as they closely resemble its real operating

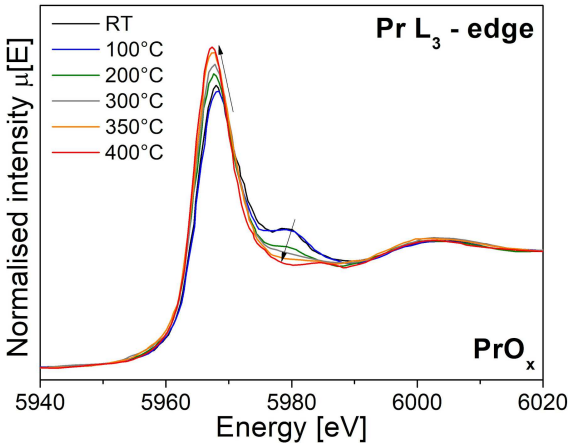

Fig. 5. XANES spectra obtained during in-situ measurements for Pr L_3-edge praseodymium oxide layer deposited on YSZ.

conditions. In this case, the potential application of praseodymium oxide as an active material for oxygen electrodes in solid oxide fuel cells (SOFCs) is considered. Figure 5 shows XANES spectra obtained for a thin film of praseodymium oxide over the temperature range from room temperature (RT) to 400°C. With increasing temperature, the white line becomes more intense and shifts to lower energy, which indicates a decrease in the average oxidation state of Pr, i.e., an increase in the Pr^{3+} fraction relative to Pr^{4+}. In parallel, the intensity of the peak at ≈ 5980 eV decreases; this feature, when compared with Pr^{3+}/Pr^{4+} reference compounds, is attributed to Pr^{4+}, and its attenuation therefore supports the reduction of Pr in the film.

To comprehensively analyse the changes occurring in the material with increasing temperature, spectral fitting was performed to determine the average oxidation state. When interpreting the spectrum, the specific electronic structure of praseodymium must be taken into account. The complexity of the spectrum results from the coexistence of Pr^{3+} and Pr^{4+} in the compound. The most intense peak at ≈ 5967 eV arises from Pr^{3+}. Moreover, a component appears on the high-energy slope (i.e., peak in the range of 5970–5971 eV), together with a third contribution at 5979 eV. These features are characteristic of Pr^{4+} states, in particular those associated with the $4f^1$ and $4f^2\underline{L}$ electronic configurations, where $\underline{L}$ denotes a ligand hole in the O $2p$ orbital. The determination of the average oxidation state of the praseodymium cations was carried out using a model consisting of the sum of four Gaussian functions and an arctangent function representing the step-like onset of continuum excitations. The first function, i.e., Gaussian A, corresponds to the pre-edge region. Gaussian B (peak at 5966 eV) represents the excitation from $2p_{3/2}$ to $4f^25d^*$ and is attributed to Pr^{3+} ions; here,

TABLE I

Calculated values from the peak fitting used to determine the average oxidation state of the praseodymium cation.

		Temperature [°C]					
		RT	100	200	300	350	400
Peak A	height	1.157 ± 0.082	0.850 ± 0.069	1.315 ± 0.077	1.569 ± 0.078	1.391 ± 0.074	0.951 ± 0.060
	position	5959.60	5959.86	5959.71	5959.45	5959.98	5959.14
	sigma	3.728	2.179	3.413	3.731	3.263	2.602
Peak B	height	6.862 ± 1.053	7.588 ± 1.126	10.030 ± 2.026	10.845 ± 0.527	12.687 ± 0.490	13.310 ± 0.226
	position	5967.25 ± 0.62	5967.03 ± 0.53	5967.00 ± 0.63	5967.19 ± 0.67	5967.08 ± 0.19	5967.20 ± 0.12
	sigma	2.911	2.911	2.893	2.938	2.895	2.837 ± 0.282
Peak C	height	4.877 ± 1.216	3.273 ± 1.120	2.732 ± 1.978	2.317 ± 0.581	1.712 ± 0.485	0.997 ± 0.232
	position	5969.42 ± 0.83	5969.71 ± 0.62	5970.19 ± 1.14	5971.32 ± 0.67	5972.15	5974.39 ± 0.46
	sigma	3.524	2.497 ± 0.287	2.999 ± 0.887	2.793	3.113 ± 0.499	2.502 ± 0.282
Peak D	height	$1.692 \pm 0.0.234$	2.290 ± 0.169	1.354 ± 0.243	0.646 ± 0.216	0.179 ± 0.092	–
	position	5978.89	5978.28	5978.18	5979.73	5982.37	–
	sigma	2.968 ± 0.257	3.682 ± 0.356	3.728 ± 0.700	3.145 ± 1.037	2.737	–
arctan	height	0.93	0.93	0.88	0.88	0.88	0.85
	position	5964.68	5964.68	5964.72	5964.43	5965.14	5964.29
	width	1	1	1	1	1	1
Average oxidation state		3.49	3.41	3.29	3.21	3.18	3.06

$5d^*$ denotes the presence of an excited electron in the $5d$ band. The remaining Gaussian components, C and D (peak in the range of 5970–5971 eV and peak at 5979 eV), correspond to excitations from $2p_{3/2}$ to $4f^2\underline{L}5d^*$ and $4f^15d^*$, respectively. Gaussian components C and D thus correspond to Pr^{4+} ions. Table I presents the resulting average oxidation states of Pr obtained using this fitting procedure. The integrated areas of the characteristic electronic–transition peaks — labelled as B (Pr^{3+}), C, and D (Pr^{4+}) — were used to calculate the praseodymium cation's average oxidation state. This was done according to

$$\mathrm{Pr_{average}} = 3\frac{\mathrm{A}\left(\mathrm{Pr^{3+}}\right)}{\mathrm{A}\left(\mathrm{Pr^{3+}}\right)+\mathrm{A}_1\left(\mathrm{Pr^{4+}}\right)+\mathrm{A}_2\left(\mathrm{Pr^{4+}}\right)} + 4\frac{\mathrm{A}_1\left(\mathrm{Pr^{4+}}\right)+\mathrm{A}_2\left(\mathrm{Pr^{4+}}\right)}{\mathrm{A}\left(\mathrm{Pr^{3+}}\right)+\mathrm{A}_1\left(\mathrm{Pr^{4+}}\right)+\mathrm{A}_2\left(\mathrm{Pr^{4+}}\right)} = 3+\frac{\mathrm{A}_1\left(\mathrm{Pr^{4+}}\right)+\mathrm{A}_2\left(\mathrm{Pr^{4+}}\right)}{\mathrm{A}\left(\mathrm{Pr^{3+}}\right)+\mathrm{A}_1\left(\mathrm{Pr^{4+}}\right)+\mathrm{A}_2\left(\mathrm{Pr^{4+}}\right)}, \quad (1)$$

where $\mathrm{A(Pr^{3+})/A_1(Pr^{4+})/A_2(Pr^{4+})}$ corresponds to the area under the Gaussian obtained for a given fitted peak.

The fits for the various temperatures are shown in Fig. 6. At RT, the average oxidation state of praseodymium is 3.49^+. This value differs slightly from the analogous analysis performed for the powdered material, for which a value of 3.43^+ was obtained. With further temperature increase, a systematic decrease in the average oxidation state of praseodymium was observed, and at 400°C, the value reaches 3.06^+, indicating that more than 90% of praseodymium is present in the 3^+ oxidation state.

Each line shape has an independent centroid, height, and width. Peak shapes are unit-normalised, meaning the height is uniquely the area under the peak. Sigma is the width of the Gaussian, and the position is the centre of the specific peak.

The use of praseodymium oxide for in-situ measurements highlights the changes occurring in the material and demonstrates the potential of measurements performed under conditions closer to those during operation. This is related to the ease with which praseodymium undergoes transitions between Pr^{4+} and Pr^{3+} and to the intrinsically non-ideal stoichiometry of praseodymium oxides. Furthermore, increasing temperature shifts the equilibrium of the system towards a more reduced state, resulting in the formation of additional oxygen vacancies. Although this phenomenon is observed in many oxide systems, in the case of PrO_x, high-temperature X-ray diffraction studies and thermogravimetric measurements of the Pr–O system performed by Burnham et al. have shown that, at constant oxygen pressure (e.g., in air), increasing temperature induces a sequence of phase transitions: $PrO_2 \rightarrow Pr_6O_{11} \rightarrow$ more reduced phases approaching Pr_2O_3. This corresponds to the gradual loss of lattice oxygen and a decrease in the average

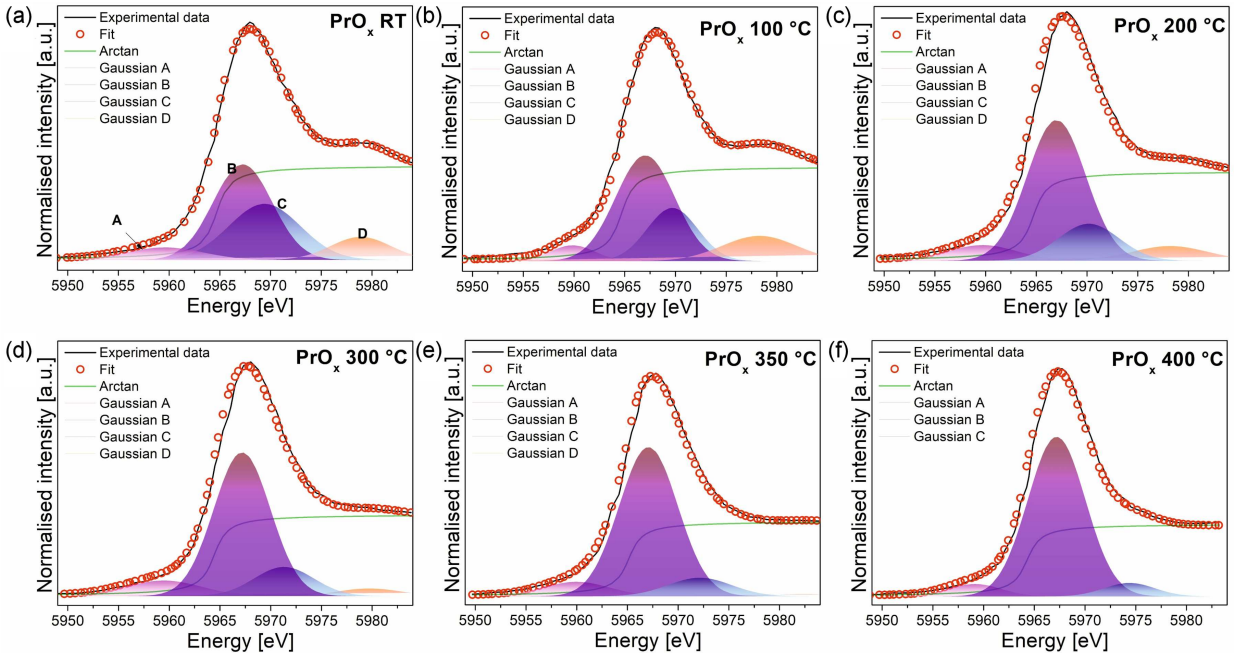

Fig. 6. Fits of spectra collected at various temperatures from RT up to 400°C using the peak fitting method.

oxidation state of praseodymium from values close to 4^+ towards 3^+ [33]. From the perspective of defect chemistry, this behaviour can be described by an equilibrium in which two Pr^{4+} cations and a regular lattice oxygen ion are transformed into two Pr^{3+} cations, one doubly positively charged oxygen vacancy, and half an oxygen molecule released into the gas phase. The large entropy increase associated with the formation of gaseous O_2 means that, at constant $p(O_2)$, the more reduced state becomes thermodynamically more favourable as temperature increases. Thermodynamic and electrical conductivity measurements confirm that the fraction of Pr^{3+} increases with temperature in air, accompanied by an increase in the concentration of oxygen vacancies [28, 34]. The pronounced reduction in the average oxidation state of praseodymium in the relatively low temperature range analysed in this work may occur due to two factors. One is the small thickness, and the second is the large surface area of the layer, which accelerates the formation of oxygen vacancies. This change directly affects both the ionic and electronic conductivity of the compound, as well as the rate of surface oxygen exchange. The observed changes in praseodymium oxide, as a mixed ionic–electronic conductor, indicate a significant increase in the concentration of oxygen vacancies in the structure, leading to an enhancement of the ionic conductivity of the material. At the same time, the increased fraction of praseodymium in the 3^+ oxidation state affects the electronic transport. In this case, the observed behaviour reduces the number of Pr^{3+}/Pr^{4+} pairs that are responsible for small-polaron transport, which contributes to a decrease in hole-type electronic conductivity.

4. Conclusions

The measuring cell prepared for in-situ and, ultimately, operando measurements was tested in the temperature range from room temperature to 400°C using hard X-ray absorption spectroscopy (XAS). To the best of our knowledge, this is the first such detailed analysis performed for the SOC electrode. Previous studies did not investigate in such detail the influence of measurement temperature on the properties of the material using XAFS in the tender and hard energy range. In the work by Fujimaki et al. [16], the beam probed the electrode along a distance profile from the electrolyte, which enabled the determination of the active surface of the electrode. In our work, a complementary geometry was used, in which a wide surface of the pellet with the electrode material deposited was directed towards the beam to prioritise the study of the material's properties and to cover a larger area of the electrode, which facilitated the observation of additional phenomena occurring at the electrode.

A pronounced decrease in the average oxidation state of praseodymium in praseodymium oxide at elevated temperature was observed, from 3.49^+ at room temperature to 3.06^+ at 400°C. The room-temperature value was consistent with that obtained from ex-situ measurements. This change was considerable and may be attributed to the low thickness of the electrode and its large contact area with air, which can accelerate reduction and oxygen release. This evolution directly affects both the electrical and ionic transport properties of praseodymium oxide. Lowering the average

oxidation state increases the concentration of oxygen vacancies, thereby facilitating faster oxygen transport, while simultaneously reducing the electronic conductivity of this mixed conductor.

The in-situ measurements presented in this work represent an important step towards enabling operando experiments and extending the accessible temperature range to 600–650°C. Furthermore, each individual stage contributes to the standardisation and validation of the measurement methodology, with the aim of developing a comprehensive and robust approach that allows operando measurements to be performed on a wide range of materials, thus opening a new field of application for XAFS. At the same time, these developments extend the capabilities of the ASTRA beamline at the SOLARIS Synchrotron and can serve as a reference for similar efforts at other synchrotron facilities.

Acknowledgments

This research has been supported by the National Science Centre (NCN) DAINA 2 project no. UMO-2020/38/L/ST8/00513: "Porous metal supported micro-scale solid oxide fuel cells: fundamentals, fabrication and testing". The XAFS measurements at ASTRA beamline at NSRC SOLARIS were made under the provision of the Polish Ministry of Science and Higher Education project "Support for research and development with the use of research infrastructure of the National Synchrotron Radiation Centre SOLARIS" under contract no. 1/SOL/2021/2. The further development of the ASTRA beamline at NSRC SOLARIS was supported within the EU Horizon 2020 program (952148-Sylinda).

References

[1] M. Singh, D. Zappa, E. Comini, *Int. J. Hydrogen Energy* **46**, 27643 (2021).

[2] A. Talukdar, A. Chakrovorty, P. Sarmah, P. Paramasivam, V. Kumar, S. Kumar Yadav, S. Manickkam, *Int. J. Energy Res.* **2024**, 6443247 (2024).

[3] J. Li, J. Cheng, Y. Zhang, Z. Chen, M. Nasr, M. Farghali, D.W. Rooney, P.-S. Yap, A.I. Osman, *Adv. Energy Sustain. Res.* **5**, 2400132 (2024).

[4] F. Ferrete, A. Molina, G.M. Cabello González, Á. Moreno-Racero, H. Olmedo, A. Iranzo, *Processes* **13**, 2656 (2025).

[5] M. Yousaf, Y. Lu, M. Akbar, L. Lei, S. Jing, Y. Tao, *Mater. Today Energy* **44**, 101633 (2024).

[6] E.D. Wachsman, K.T. Lee, *Science* **334**, 935 (2011).

[7] A. Tarancón, *Energies* **2**, 1130 (2009).

[8] A. Stangl, D. Muñoz-Rojas, M. Burriel, *J. Phys. Energy* **3**, 012001 (2021).

[9] Z. Ma, C. Chatzichristodoulou, F.M. Chiabrera, K.S. Mřlhave, S.B. Simonsen, *ACS Energy Lett.* **9**, 2007 (2024).

[10] J.B. Kowalski, W. Paszkowicz, R. Nietubyć, E. Guziewicz, Z. Kaszkur, *Promieniowanie Synchrotronowe w Fizyce i Chemii Ciała Stałego*, 1st ed., Adam Mickiewicz University Press, 2024.

[11] B. Lemieszek, M. Ilickas, J. Jamroz et al., *Appl. Surf. Sci.* **670**, 160620 (2024).

[12] K. Amezawa, *Curr. Opin. Electrochem.* **21**, 250 (2020).

[13] H. Funke, A.C. Scheinost, M. Chukalina, *Phys. Rev. B* **71**, 094110 (2005).

[14] H. Funke, M. Chukalina, A.C. Scheinost, *J. Synchrotron Radiat.* **14**, 426 (2007).

[15] L.M. Acuña, M.D. Cabezasa, R.O. Fuentes *Energy Adv.* **1**, 344 (2022).

[16] Y. Fujimaki, T. Nakamura, Y. Kimura, K. Nitta, O. Sekizawa, Y. Terada, K. Yashiro, T. Kawada, K. Amezawa, *J. Phys. Chem. Lett.* **16**, 9599 (2025).

[17] K. Zielińska, J. Dąbrowa, M. Zajusz, M. Szymczak, K. Li, P. Winiarz, M. Gajewska, K. Świerczek, *Chem. Eng. J.* **504**, 158974 (2025).

[18] C. Lei, M.F. Simpson, A.V. Virkar, *J. Electrochem. Soc.* **169**, 104506 (2022).

[19] J. Januschewsky, M. Kubicek, M. Stoeger-Pollach, J. Bernardi, J. Fleig, *ECS Trans.* **25**, 2397 (2009).

[20] P. Hjalmarsson, M. Sřgaard, M. Mogensen, *Solid State Ionics* **179**, 1422 (2008).

[21] M. Sřgaard, P.V. Hendriksen, M. Mogensen, F.W. Poulsen, E. Skou, *Solid State Ionics* **177**, 3285 (2006).

[22] Y.T. Kim, N. Shikazono, *Solid State Ionics* **319**, 162 (2018).

[23] V. Vibhu, S. Yildiz, I.C. Vinke, R.A. Eichel, J.M. Bassat, L.G.J. de Haart, *J. Electrochem. Soc.* **166**, F102 (2019).

[24] S.P. Simner, J.F Bonnett, N.L Canfield, K.D Meinhardt, J.P Shelton, V.L Sprenkle, J.W Stevenson, *J. Power Sources* **113**, 1, (2003).

[25] W.-H. Kim, H.-S. Song, J. Moon, H.-W. Lee, *Solid State Ionics* **177**, 3211 (2006).

[26] Z. Zhao, L. Liu, X. Zhang, W. Wu, B. Tu, D. Cui, D. Ou, M. Cheng, *Int. J. Hydrogen Energy* **38**, 15361 (2013).

[27] J. Hayd, E. Ivers-Tiffée, *J. Electrochem. Soc.* **160**, F1197 (2013).

[28] S. Ferro, *Int. J. Electrochem.* **2011**, 561204 (2011).

[29] E.S. Putna, J.M. Vohs, R.J. Gorte, G.W. Graham, *Catal. Letters* **54**, 17 (1998).

[30] V. Thangadurai, R.A. Huggins, W. Weppner, *J. Solid State Electrochem.* **5**, 531 (2001).

[31] B. Lemieszek, L. Alluhaibi, A. Maximenko et al., *Chem. Eng. J.* **531**, 173949 (2026).

[32] B. Ravel, M. Newville, *J. Synchrotron Radiat.* **12**, 537 (2005).

[33] D.A. Burnham, L.R. Eyring, *J. Phys. Chem.* **72**, 4415 (1968).

[34] P. Sonström, J. Birkenstock, Y. Borchert, L. Schilinsky, P. Behrend, K. Gries, K. Müller, A. Rosenauer, M. Bäumer, *ChemCatChem* **2**, 694 (2010).